The impact of Al/Cr ratio on the oxidation kinetics of Y-doped AlCoCrFeNi high-entropy alloys at 1100 °C

Intermetallics 176 (2025) 108582

Contents lists available at ScienceDirect

Intermetallics

journal homepage: www.elsevier.com/locate/intermet

The impact of Al/Cr ratio on the oxidation kinetics of Y-doped AlCoCrFeNi high-entropy alloys at 1100 °C

Xiaoyu Sun [a], Xiaolong Li [b], Sheng Guo [b], Lilong Zhu [c], Jianwei Teng [c], Liang Jiang [c], Johan Moverare [a], Xin-Hai Li [d], Ru Lin Peng [a,*]

[a] Department of Management and Engineering, Linköping University, SE-58183, Linköping, Sweden
[b] Department of Industrial and Materials Science, Chalmers University of Technology, SE-41296, Gothenburg, Sweden
[c] Institute for Advanced Studies in Precision Materials, Yantai University, 264005, Yantai, China
[d] Siemens Energy AB, SE-61283, Finspång, Sweden

ARTICLE INFO

Keywords:
Oxidation kinetics
High-entropy alloy
Thermodynamic calculations

ABSTRACT

Y/Hf-doped AlCoCrFeNi high-entropy alloys stand out for their potential application in high temperature coatings. Thereinto, both Cr and Al are crucial for improving oxidation properties. However, simultaneously increasing the content of Al and Cr is not advisable, since it can significantly reduce the ductility/toughness of the coating. In this research, we proposed an equivalent replacement method of Al and Cr, namely, tuning Al/Cr ratio (ACR), to enhance the elevated-temperature oxidation resistance of AlCoCrFeNi alloys. This strategy was verified by the 1000 h/1100 °C oxidation tests of three Y-doped AlCoCrFeNi alloys with different ACRs of 0.78, 0.58 and 0.41. The test results indicated an elusive transformation of oxidation rate occurred on these alloys, that the alloy with lowest ACR exhibited an initially higher oxidation rate but a lower oxidation rate over an extended period, in comparison to those higher ACR alloys. The underlying oxidation mechanisms were uncovered using microscopic techniques and thermodynamics calculations. The initial higher oxidation rate was ascribed to the rapid growth of spinel oxides, while the extended slower oxidation process was attributed to the resulting Al_2O_3 scale with larger grain sizes. Thermodynamic assessment revealed that larger Al_2O_3 grains corresponding to fewer grain boundaries decreased the diffusion coefficient of oxygen in Al_2O_3 scale. Our research is of both theoretical and industrial importance for clarifying the high temperature oxidation mechanism of Y-doped AlCoCrFeNi alloys and enhancing the oxidation resistance in multicomponent alloy systems.

1. Introduction

Y/Hf-doped AlCoCrFeNi high-entropy alloys (HEAs) have attracted increasing attention for their potential application in high temperature coatings [1–4]. In comparison with classic MCrAlY (M: Ni and/or Co) alloys, these materials display lower oxidation rate and superior resistance to oxide-layer spallation, which have been substantiated by long-term high-temperature oxidation tests [5–8]. Their superior oxidation properties can be primarily attributed to the resulting Al_2O_3 layer with large grain-size and the beneficial reactive-element effect [7–11]. More specifically, the presence of Fe and high Al content facilitate the early establishment of Al_2O_3 through increasing the Al activity [7,8,12]; the formed large grain-size structure reduces the number of grain boundaries that act as fast diffusion pathways for oxygen. Reactive elements such as Y and Hf enhance the bonding force between oxide layers and the underlying alloys or coatings [6,7,10,11]. However, current research tends to neglect the effect of Cr in this system. During the oxide-forming process, Al and Cr are pivotal contributors [13–15]. The outward diffusion of Al and Cr results in the formation of the principal oxide layers as oxidation barrier by selective oxidation. According to the classic oxidation theories of metals, Cr acts as an oxygen getter and promotes the phase transition from γ-Al_2O_3 to dense α-Al_2O_3 [16–18]. Cr is also found to prevent internal oxidation of Al and help to maintain an intact Al_2O_3 layer [17,19,20]. Thus, the effects of both Cr and Al should be considered for improved oxidation properties. Unfortunately, simultaneously increasing the content of Al and/or Cr is not advisable, since it can significantly reduce the ductility or toughness of coatings [16].

In this research, we investigated the isothermal oxidation behaviors of three Y-doped AlCoCrFeNi HEAs with varying Al/Cr ratios (ACRs) at

* Corresponding author.
E-mail address: ru.peng@liu.se (R.L. Peng).

https://doi.org/10.1016/j.intermet.2024.108582
Received 3 September 2024; Received in revised form 18 November 2024; Accepted 23 November 2024
Available online 29 November 2024

1100 °C in air for 1000 h, using multiple microscopic techniques and thermodynamic calculations. 1100 °C was chosen as the test temperature, as it is the highest operating temperature for the existing coated-superalloy systems [21]. The experimental results indicated that the oxidation rate increased with the increase of ACR for the long-term oxidation, whereas an opposite trend was observed during the early stage. We studied the formed oxides on the surface of alloys, uncovering that the oxidation process at the very early stage was dominated by the fast spinel growth, while Al_2O_3 of large grain size formed on the lower ACR alloy helped to reduce the inward diffusion of oxygen and thus decrease the oxidation rate.

2. Experiments

HEA ingots with a size of 10 × 10 × 25 mm^3 were prepared using high purity (>99.9 %) pure metals by arc melting technology, in a water-cooled copper mold with Ar protective atmosphere. The compositions of three HEAs are listed in Table 1. The ingots were sliced into pieces (2 × 10 × 25 mm) for oxidation tests, by the means of electrical discharge machining (EDM). Before oxidation, the surface of each specimen was sequentially ground by #400, #800 and #1200 SiC sandpapers. Corundum crucibles were chosen as the container, and they were heated up to 1100 °C for 200 h prior to oxidation tests to remove potentially volatile matters. Oxidation tests were carried out at 1100 °C in air, using a laboratory furnace to study the long-term oxidation kinetics for up to 1000 h and a thermal analyzer (STA, STA 449) with a precision of 0.001 mg to obtain the initial oxidation kinetics for 1 h. During the long-term tests, three samples for each HEA were used to obtain the weight-change curves. These measurements were taken using a precision balance (0.01 mg) at the interval of 50 h of oxidation time.

After the oxidation tests, the specimens were electroless plated with a 1–2 μm thick nickel film to protect the oxide scales, mounted in resin and then polished. The microstructures of HEAs and the formed oxide layers were examined using X-ray diffraction (XRD, PANalytical X'Pert Pro) and scanning electron microscope (SEM, Hitachi SU70 FEG) equipped with energy dispersive X-ray spectroscopy (EDS) and wavelength dispersive spectroscopy (WDS). The acceleration voltage was 15 KV. The working distance (WD) was approximately 15 mm.

Prior to conducting EDS or WDS, the standardization database was calibrated using Oxford standard blocks.

3. Results and discussions

3.1. Microstructures of Y-doped AlCoCrFeNi alloys

Fig. 1 illustrates the distinct microstructures of the three HEAs attributed to variations in Al and Cr contents. The examined results from XRD and EDS reveal that the alloys are composed of a γ phase (face-centered cubic crystal, FCC), a β phase (body centered cubic crystal, BCC) and disperse distributed Y-rich particles. The EDS maps highlight the enrichment of Ni, Al in the β phase and enrichment of Co, Cr, Fe in the γ phase. The D741 alloy with the highest ACR (0.78) comprises a β matrix and bimodal γ precipitates, namely an almost continuous network of thick γ and small, elongated γ grains in the β matrix (Fig. 1a and b). The phase fractions of β and γ are 53.9 vol% and 46.1 vol%, respectively, which are measured by the image segmentation method [22]. With a lower ACR of 0.58, the small, elongated γ grains are missing in D742 and its microstructure consists of approximately 44.8 vol % β and 55.2 vol % γ. A classical eutectic structure featuring alternating lamellar morphology can be observed in D743 with the lowest ACR (0.41), which is composed of 30.7 vol % β and 69.3 vol% γ. To elucidate the observed distinct microstructures, thermodynamic calculations (TC, 2020b) [22–24] and differential scanning calorimetry (DSC) were carried out to investigate the phase transitions during the solidification process (Fig. 2). As the temperature decreased, β was the primary phase to precipitate from liquid (L→ β + L), aligning with the first peak in the DSC results (D741 and D742). It was evident that a reducing ACR could lower the initial precipitation temperature of β (1426 °C for D741, 1377 °C for D742 and 1335 °C for D743). Subsequently, at the second peak (about 1335 °C) in D741 and D742, a eutectic reaction occurred, L → β + γ, with significantly enthalpy changes (see Fig. S1 in Supplementary materials). In D741, the eutectic reaction took place at primary solidification stage, when β and γ simultaneously precipitated from L, resulting in the alternating lamellar microstructure (see Fig. 1e and f).

Table 1
Composition (in wt.%) of three as-cast HEAs with different Al/Cr ratio (ACR), measured by WDS.

	Al	Cr	Fe	Co	Ni	Y	ACR
D741	12.05	15.41	10.00	24.46	37.39	0.68	0.78
D742	10.52	18.15	9.66	24.00	37.02	0.65	0.58
D743	8.69	20.95	9.66	23.76	36.30	0.63	0.41

3.2. Oxidation behaviors

Fig. 3a depicts the weight gains per unit area (*W*) of D741, D742 and D743 HEAs as a function of oxidation time at 1100 °C spanning up to 1000 h, indicating a clear declining trend of oxidation rate with oxidation time. Hence, parabolic kinetics were employed to describe the weight-gain processes. The inset of Fig. 3a suggests the relations between the square of weight gain and oxidation time, in which the slope of the curve, that indicates the oxidation rate, is found to decrease for all the three alloys after approximately 150 h.

Due to the change in slope, each oxidation process is divided into two stages, both described by the parabolic law [16,25,26] but with different parameters:

$$W^2 = k_p t + C \quad (1)$$

where k_p and t are parabolic parameter and oxidation time, respectively. C is a fitting constant. The constant C is needed for the parabolic fitting, since there is a linear stage prior to the parabolic stage during the oxidation process [19,27,28]. The constant C is related to the transition time from the linear stage to the parabolic stage [19,27,28]. At the initial stage, the fitted k_p of D741, D742 and D743 HEAs is 0.0037, 0.0060 and 0.0038 $mg^2cm^{-4}h^{-1}$, respectively. After the transition point, the oxidation rate is significantly decreased and the corresponding k_p value of the three HEAs is 0.0018, 0.0017 and 0.0008 $mg^2cm^{-4}h^{-1}$, respectively.

Typically, a higher Al content in alloy is expected to reduce the oxidation rate [2,8]. However, this work indicates that the ACR ratio could also be important for the oxidation resistance. While D741 and D742 seem to follow the trend for the Al effect, D743 with the lowest Al content deviates from this trend. The ultimate weight gain per unit area of D743 is 1.13 mg/cm^2, which is significantly lower than that of D741 (1.40 mg/cm^2) and D742 (1.49 mg/cm^2) with higher Al contents. On the other hand, short-term oxidation tests at 1100 °C in air using a TGA reveal that the early-stage oxidation rates of these alloys increased with decreasing Al content, as shown in Fig. 3b. This means that the oxidation behaviors at the initial and long-term stages are reversed for D743 which has the lowest Al content but also the highest Cr content, namely, a low ACR. A mechanistic understanding of this finding is necessary for improving the oxidation resistance of HEA coatings. Therefore, the following sections will delve into discussing the oxidation mechanisms during both the initial and prolonged processes.

3.3. Initial oxides on the surface of HEAs

The initially formed oxides on the surface of the three HEAs upon an initial oxidation are shown in Fig. 4, revealing different oxidation mechanisms on the surface of β and γ phases. The γ phase displayed a

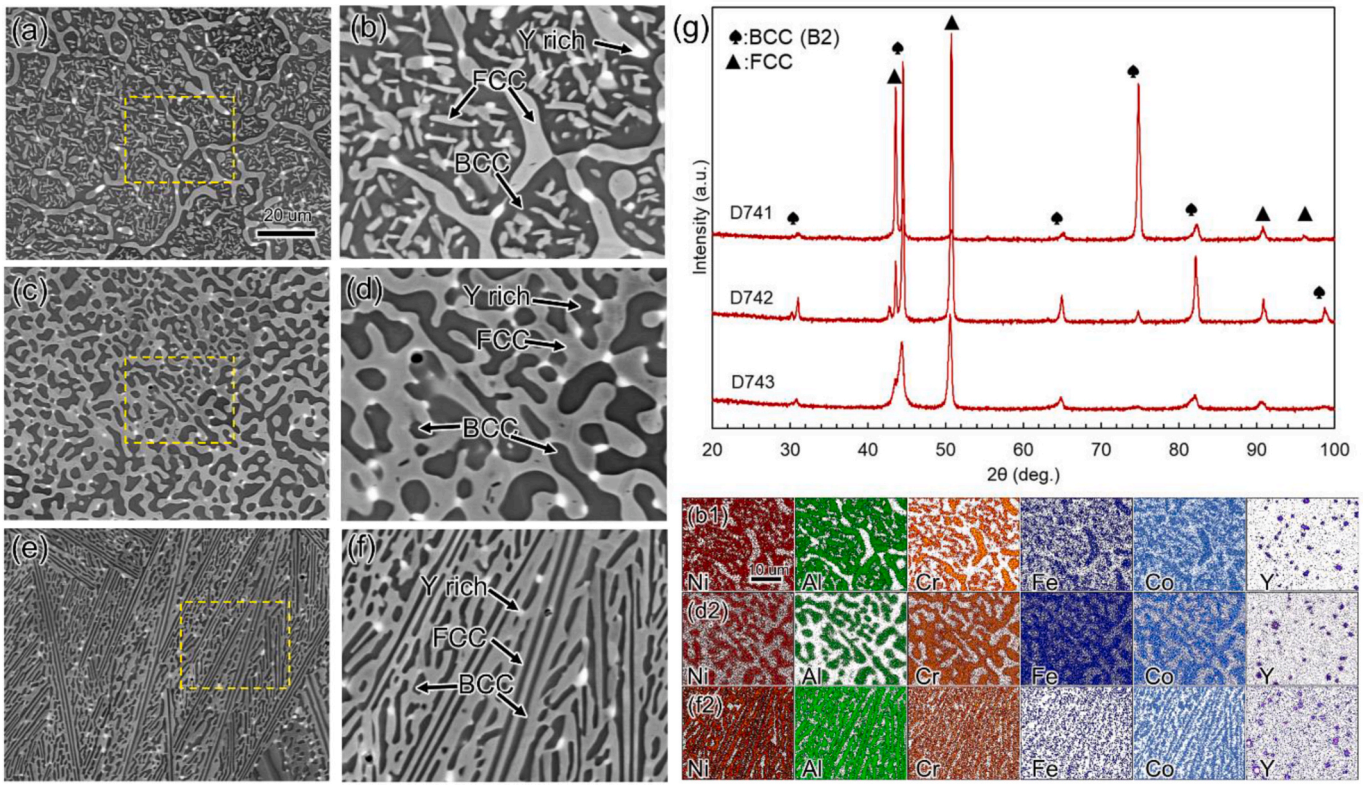

Fig. 1. Microstructure and XRD profiles of HEAs: low magnification backscattered electron (BSE) images, showing the microstructure of (a) D741, (c) D742 and (e) D743; (b, d and f) magnified BSE images of the rectangular regions marked in (a, c and e) with the corresponding EDS maps, indicating the elemental distribution; (g) XRD patterns of three as-cast HEAs.

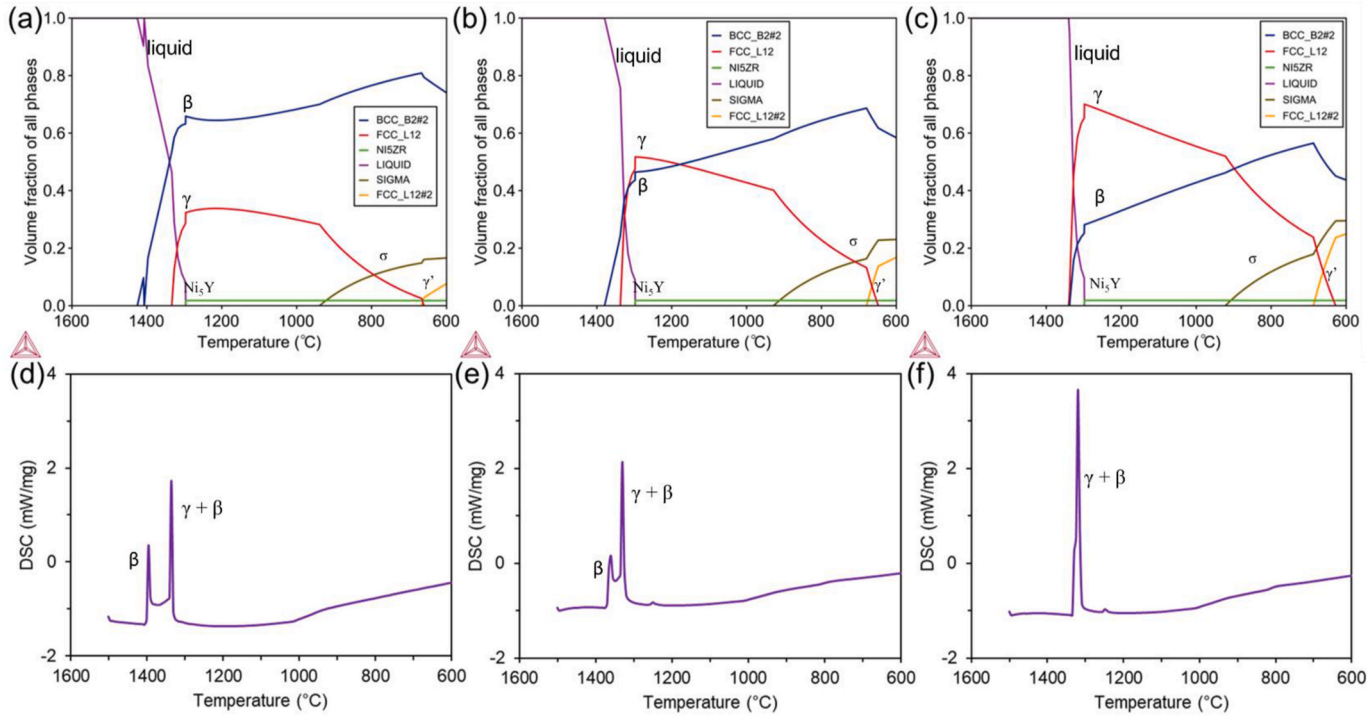

Fig. 2. The thermodynamics calculation results of phase transitions during solidification processes from 1500 °C to 600 °C in (a) D741, (b) D742 and (c) D743, which were also verified using DSC, given in (d) D741, (e) D742 and (f) D743.

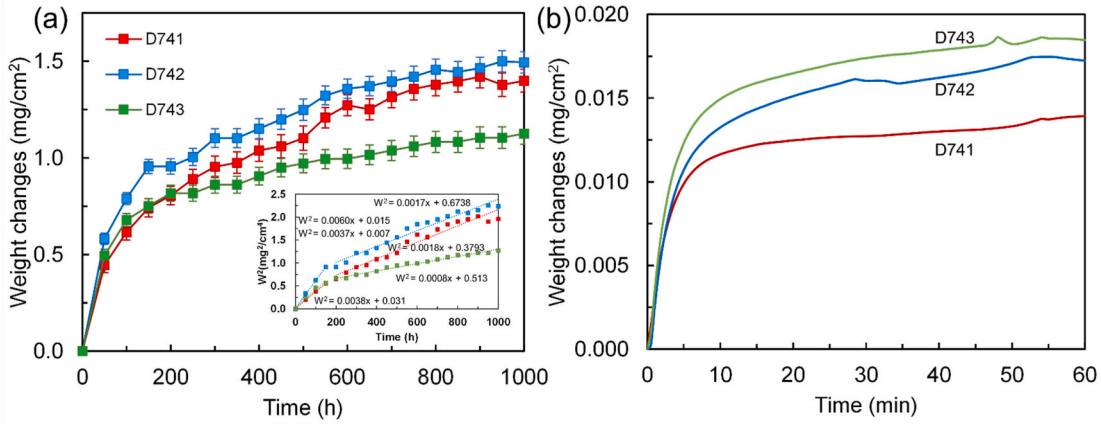

Fig. 3. (a) Weight-change curves of D741, D742 and D743 HEAs as a function of oxidation time during 1100 °C/1000 h oxidation tests, measured by a precision balance; (b) Initial oxidation kinetics of D741, D742 and D743 HEAs for 1 h, measured by a simultaneous thermal analyzer. The error bar is the standard deviation of three samples for each HEA.

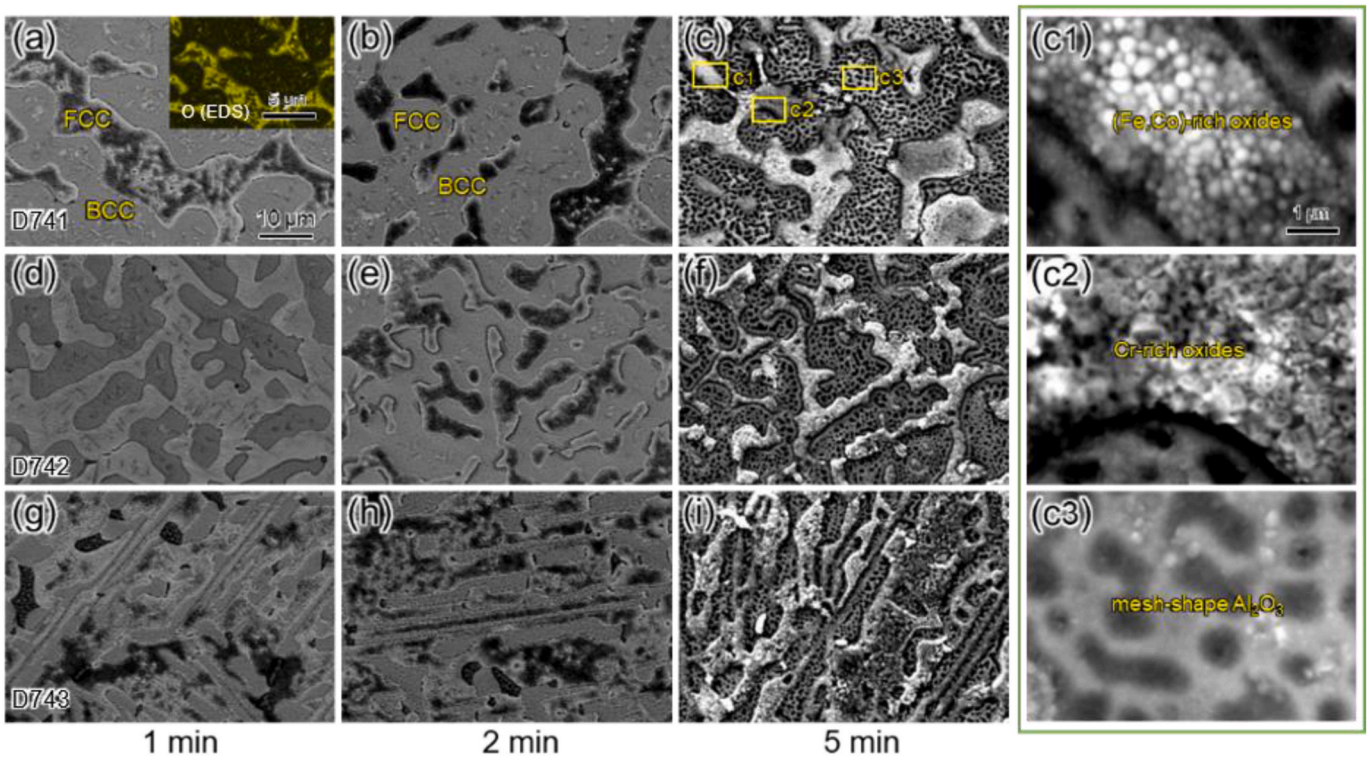

Fig. 4. Microstructural evolution on the surface of (a–c) D741, (d–f) D742 and (g–i) D743 HEAs, during the initial oxidation stage at 1100 °C.

prominent oxidation with a significant enrichment of oxygen element (see the inset of Fig. 4a). The oxides covering the γ regions were mainly composed of spherical Fe and/or Co-rich oxides and cube-shaped Cr-rich oxides, as shown in Fig. 4 c1, c2 and Supplementary Fig. S2. The β sections were covered by mesh-shape Al_2O_3 layers (see Fig. 4 c3 and Supplementary Fig. S2), and the observed contrast was ascribed to undulate morphology. It is established that the growth of Al_2O_3 is comparatively slower than that of other oxides, owing to its large bandgap (over 6 eV) and consequently a lower electron migration rate [16,29]. The initial oxidation kinetics of D741, D742 and D743 could be elucidated by the different oxidation behavior of the β and γ phase. Specifically, the HEA with a higher ACR had a high phase fraction of the β phase, characterized by a lower oxidation rate, as more Al_2O_3 with a slow growth rate was formed on the β phase surface. Accordingly, the oxidation rate of D741 with a high ACR and a high β phase fraction was the lowest in these three alloys, which was corroborated by the TGA test (see Fig. 4b).

3.4. Prolonged oxidation kinetics

Fig. 5 illustrates the evolution of oxide scales of the three HEAs during the long-term oxidation tests at 1100 °C. Double oxide layers formed on the surface of oxidized HEAs: thin spinel and Al_2O_3 layer formed on D741 and D742, and thick spinel layer and thinner columnar Al_2O_3 layer formed on D743, as shown in Fig. 4a–i and Supplementary Fig. S3. During the extended oxidation period, the weight gain primarily stemmed from the growth of Al_2O_3, supported by the comparison of the oxide layer thickness evolution between Al_2O_3 and spinel shown in Fig. 6. (Y, Al)-rich and Y-rich oxides could be detected in the Al_2O_3 layer and the substrate, as evident in Fig. 5d–m and n. The original Y-rich

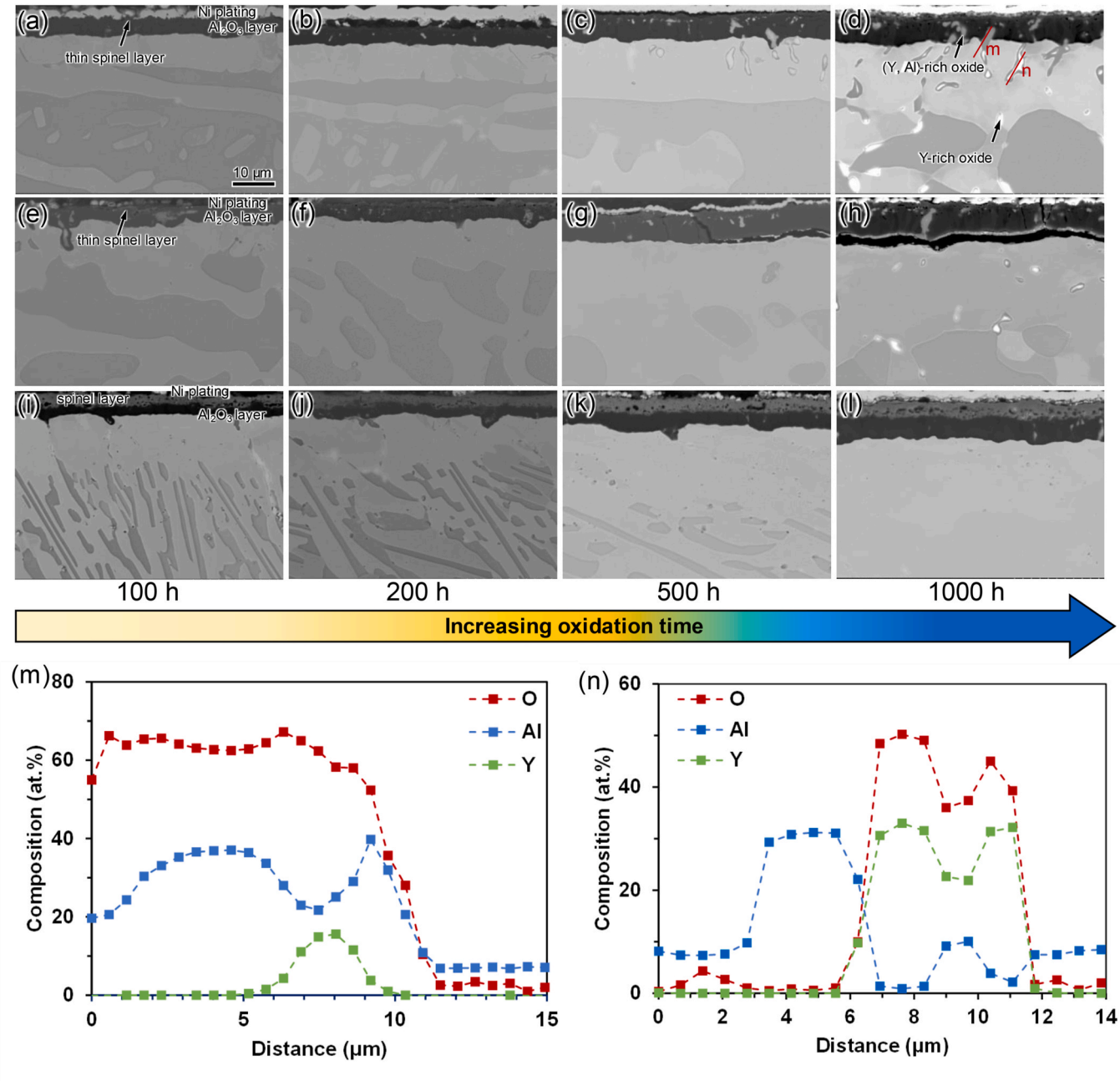

Fig. 5. The evolution of oxide layers on the surface of (a–d) D741, (e–h) D742 and (i–l) D743 HEAs during the 1000 h oxidation process at 1100 °C; EDS lines scans of Y-rich oxides measured on the oxide layers (m) and substrate (n) in D741 (d).

particles were found to dissolve within the inner of alloys after 50 h, as depicted in the inner of HEAs (Fig. 5a–e and i). Here, one role Y played here is to enhance the bonding force between the formed Al_2O_3 layer and HEAs. Y could segregate to the interface and improve the oxide-scale adhesion by the pegging effect [16]. This pegging behavior can be found near the oxide/metal interface in Fig. 3, where the outward diffusing Y reacted with oxygen and/or Al_2O_3, forming (Y, Al)-rich oxides. Fig. 7 displays the cross-sectional morphologies of Al_2O_3 formed on the HEAs at 1100 °C after 10 h and 1000 h of oxidation, revealing that the grain size of Al_2O_3 on D743 is significantly larger than that on D742 and D741. This means fewer grain boundaries formed in the Al_2O_3 layer on D743. According to previous research, grain boundaries can provide fast diffusion paths for oxygen [30]. Since the dynamic segregation effect of reactive element Y inhibits the outward diffusion of metal cations, the growth of Al_2O_3 layer is dominated by the transport of oxygen anions [31–33]. Therefore, the larger grain size signifies a lower diffusion rate of oxygen and a lower growth rate of Al_2O_3.

To verify the effect of the Al_2O_3 grain size on oxidation, Wagner's oxidation theory is employed to derive the growth kinetics of the Al_2O_3 layer guided on the following assumptions: (a) The oxidation reaction of Al element is under thermodynamic equilibrium; (b) Since Al_2O_3 is an n-type oxide and the reactive element Y inhibits the outward diffusion of metal ions, only the transport of oxygen anions in the Al_2O_3 layer is considered; (c) The diffusion path of oxygen ions includes the crystal lattices and grain boundaries, but the dislocations in Al_2O_3 are neglected.

A general oxidation reaction of metal element M can be expressed as:

$$\frac{2x}{y}M(s) + O_2(g) = \frac{2}{y}M_xO_y\ (s) \tag{2}$$

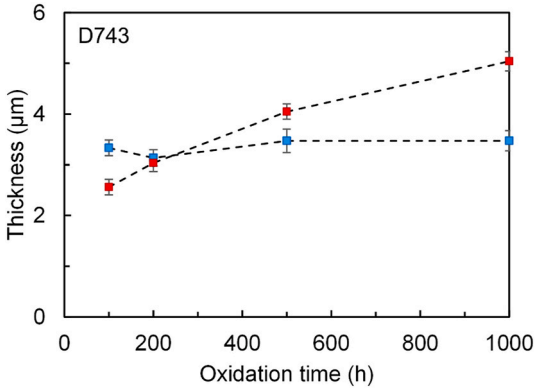

Fig. 6. The growth of Al_2O_3 and spinel layers on the D743 HEA during the 1100 °C/1000 h oxidation test. The error bar is the standard deviation of 5 measurements in different regions.

A time-depending kinetics constant k_t could be introduced from the classic Wagner's theory [25] as follows:

$$k_t = -\frac{\sigma_t t_{ion} t_{el}}{z_c^2 z_a^2 e_c^2}\Delta G_f \tag{3}$$

Where σ_t is the conductivity of the M_xO_y oxide. t_{ion} and t_{el} represent the transported numbers of ions and electrons, respectively. The valences of the metal and oxygen ions are denoted as z_c and z_a, respectively; to be consistent with the valence of oxygen, one has $z_a = -2$. The charge of species is represented by e_c. ΔG_f is the Gibb's free energy for the formation of M_xO_y oxide. Beside the transportation of ions, the Gibb's free energy for the formation of Al_2O_3 is another factor controlling the growth of Al_2O_3, since it is the driving force of the oxidation reaction, which would be increased due to the increment of Al content in HEAs with the high ACR.

Since Al_2O_3 is an n-type oxide rather than a p-type oxide, it is taken as an electron conductor with $t_{el} \approx 1$, and the conductive ions are mainly oxygen ions. Hence, the k_t can be expressed as [34]:

$$k_t = -\frac{\sigma_t t_o}{z_c^2 z_a^2 e_c^2}\Delta G_f \tag{4}$$

where t_o represents the transported number of the oxygen ions. With the use of the Nernst–Einstein relation, Eq. (4) can be rewritten as [34]:

$$k_t = -\frac{c_o}{z_c^2 kT} D_o \Delta G_f \tag{5}$$

where c_o represents the concentration of oxygen, which can be regarded as a constant in Al_2O_3, D_o represents the diffusion coefficient of oxygen in the oxide layer. According to Eq. (5), the kinetics parameter k_t is determined by the diffusion coefficient of oxygen D_o and the Gibbs free energy of formation ΔG_f.

During the reaction, the ΔG_f of M_xO_y oxide was calculated using:

$$\Delta G_f = \Delta G_0 - RT \ln\left(\frac{a_{M_xO_y}^{2/y}}{a_M^{2x/y} \bullet P_{O_2}}\right) \tag{6}$$

Where, ΔG_0 is the standard free energy of formation under the oxidation reaction. T is the absolute temperature, and R is the gas constant. $a_{M_xO_y}$ represents the activity of the oxide of metal element M. a_M is the activity of element M in the HEA which is subject to oxidation. The partial pressure of oxygen is P_{O_2} which approaches to 0.21 atm in the atmosphere. Eq. (6) can be also utilized to calculate the equilibrium partial pressure of oxygen by making ΔG_f equal to zero. ΔG_0 can be accessed from the Ellingham diagram [35] (see Supplementary Fig. S4), and a_M can be calculated using the Thermo-Calc software. The calculated ΔG_f of Al_2O_3 for D741-3 are −588.0, −587.5 and −587.2 kJ/mol, showing a slight difference with the change in ACR. It can be found that the ΔG_f of Al_2O_3 is only up to the activity of Al, when T and P_{O_2} are constant (see Eq. (6)). However, the positive effect of Al on its activity is significantly counteracted due to the decrease in Cr content, as shown in Fig. 8a and b. Thus, the ΔG_f of Al_2O_3 changes insignificantly due to the simultaneous alterations of Al and Cr contents.

For a polycrystalline Al_2O_3 layer, the overall diffusion flux of oxygen is the sum of the fluxes through the bulk lattice and grain boundary. As a result, the diffusion coefficient of oxygen in Al_2O_3 layer ($D_o^{Al_2O_3}$) can be

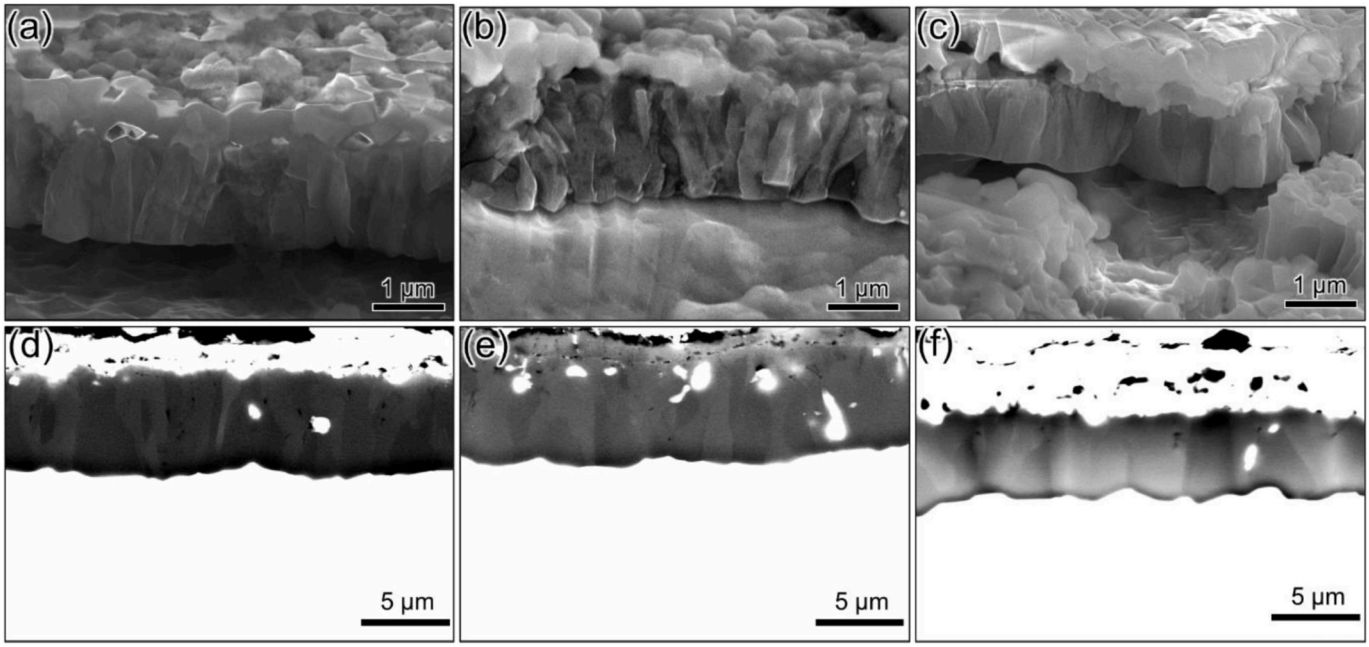

Fig. 7. The cross-sectional morphologies of oxide layers after oxidation at 1100 °C for 10 h: (a) D741, (b) D742, (c) D743, and after oxidation at 1100 °C for 1000 h: (d) D741, (e) D742, (f) D743.

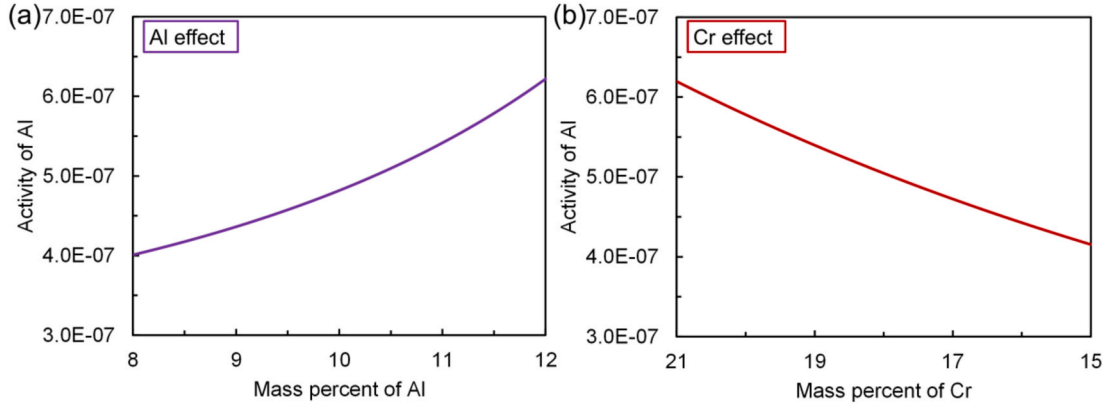

Fig. 8. The effect of (a) Al and (b) Cr on the activity at 1100 °C, calculated by TC based on the TCIN10 database.

expressed as [36,37]:

$$D_o^{Al_2O_3} = D_o^L(1-f) + D_o^{GB}f \tag{7}$$

Where, D_o^L and D_o^{GB} respectively represent the diffusion coefficient of oxygen in Al_2O_3 crystal lattice and grain boundary, obtained from Ref. [38]. f is the area ratio of the grain boundary, given by Refs. [36,37]:

$$f = \frac{2\delta}{d} \tag{8}$$

where δ is the grain boundary thickness (~0.6 nm for Al_2O_3 layer [36,37]) and d is the grain size.

Fig. 9 shows the calculated $D_o^{Al_2O_3}$ at 1100 °C, as a function of grain size, revealing that $D_o^{Al_2O_3}$ is very sensitive to the grain size, with a significant reduction in $D_o^{Al_2O_3}$ observed as the grain size increases. The calculated $D_o^{Al_2O_3}$ in the formed Al_2O_3 on D743 is approximately half that in D742 and D741 (the inset of Fig. 9), which agrees with the long-term test results (Fig. 3a). And the calculated $D_o^{Al_2O_3}$ shows a strong positive correlation with oxidation kinetic parameters (long-term stage) as illustrated in Fig. 10. This implies that the transportation of oxygen in Al_2O_3 is the critical factor for the long-term oxidation stage. Therefore, the lower oxidation rate in HEAs with low ACR is mainly ascribed to the resulting large sized Al_2O_3 grains. As fewer grain boundaries are available as fast inward diffusion path for oxygen, a lower oxygen diffusion rate is achieved, leading to a reduced growth rate of the Al_2O_3 layer.

4. Conclusions

In this research, we investigated the oxidation behaviors of three Y-doped AlCoCrFeNi HEAs with varying ACR. The oxidation tests were conducted in air at 1100 °C for up to 1000 h. The following conclusions can be reached:

(1) Diverse microstructures in the three HEAs were observed after adjusting the ACR. Phase equilibrium calculations and DSC tests indicated that decreasing the ACR could lower the initial precipitation temperature of the β phase, consequently reducing β precipitation.
(2) Microstructural analysis on the surface oxides revealed that the fast growth of spinel dominated the early oxidation process of the HEAs with lower ACR, resulting in a higher oxidation rate compared to the HEAs with higher ACR.
(3) The prolonged oxidation stage was governed by the growth of the Al_2O_3 layer, as confirmed by comparing the growth of the Al_2O_3 layer and the spinel layer. Thermodynamics assessment revealed that reducing grain boundaries in Al_2O_3 scale could decrease the diffusion coefficient of oxygen. Hence, low ACR with less Al_2O_3 grain boundaries displayed a lower oxidation rate during the prolonged oxidation stage.

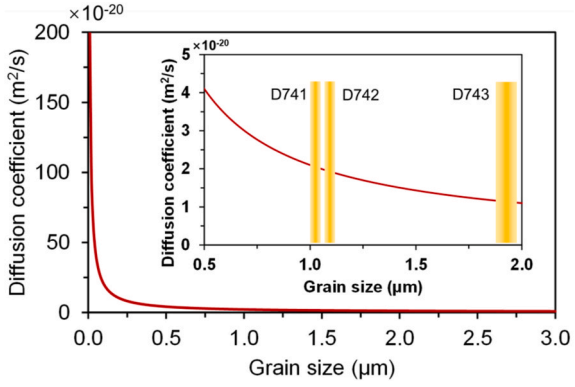

Fig. 9. Calculated diffusion coefficient of oxygen in the formed Al_2O_3 layer as a function of grain size at 1100 °C.

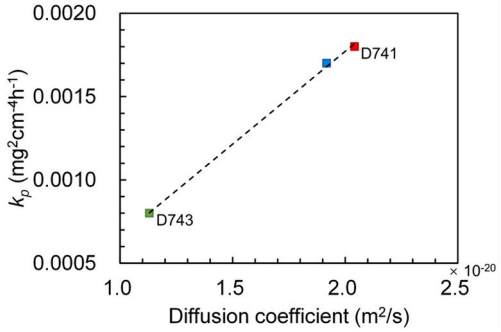

Fig. 10. The relation between the oxidation kinetic parameters (long-term stage) and the calculated diffusion coefficients of O in Al_2O_3 layer.

CRediT authorship contribution statement

Xiaoyu Sun: Writing – original draft, Validation, Software, Methodology, Investigation, Formal analysis, Conceptualization. **Xiaolong Li:** Resources, Investigation. **Sheng Guo:** Writing – review & editing, Resources, Conceptualization. **Lilong Zhu:** Resources, Investigation. **Jianwei Teng:** Writing – review & editing, Investigation, Conceptualization. **Liang Jiang:** Resources, Investigation, Conceptualization. **Johan Moverare:** Writing – review & editing, Supervision, Resources, Conceptualization. **Xin-Hai Li:** Writing – review & editing, Supervision, Resources, Conceptualization. **Ru Lin Peng:** Writing – review & editing,

Supervision, Resources, Project administration, Investigation, Funding acquisition, Conceptualization.

Data availability statement

The raw/processed data required to reproduce these findings cannot be shared at this time as the data also forms part of an ongoing study.

Declaration of competing interest

The authors declare that they have no known competing financial interests or personal relationships that could have appeared to influence the work reported in this paper.

Acknowledgements

The authors acknowledge the financial support from Siemens Industrial Turbomachinery AB (Finspång, Sweden) and Stiftelsen Axel Hultgrens Fond (Stockholm, Sweden). R. P. appreciates the Swedish Government Strategic Research Area in Materials Science on Functional Materials at Linköping University (Faculty Grant SFO-Mat-LiU 2009-00971) for financial support.

Appendix A. Supplementary data

Supplementary data to this article can be found online at https://doi.org/10.1016/j.intermet.2024.108582.

Data availability

Data will be made available on request.

References

[1] Z. Fu, L. Jiang, J.L. Wardini, B.E. MacDonald, H. Wen, W. Xiong, D. Zhang, Y. Zhou, T.J. Rupert, W. Chen, E.J. Lavernia, A high-entropy alloy with hierarchical nanoprecipitates and ultrahigh strength, Sci. Adv. 4 (2018) 1–9, https://doi.org/10.1126/sciadv.aat8712.

[2] T.M. Butler, M.L. Weaver, Oxidation behavior of arc melted AlCoCrFeNi multi-component high-entropy alloys, J. Alloys Compd. 674 (2016) 229–244, https://doi.org/10.1016/j.jallcom.2016.02.257.

[3] W. Li, P. Liu, P.K. Liaw, Microstructures and properties of high-entropy alloy films and coatings: a review, Mater. Res. Lett. 6 (2018) 199–229, https://doi.org/10.1080/21663831.2018.1434248.

[4] R. Gawel, Ł. Rogal, G. Smoła, Z. Grzesik, High-temperature oxidation and diffusion studies on selected Al–Cr–Fe–Ni high-entropy alloys for potential application in thermal barrier coatings, Intermetallics 169 (2024), https://doi.org/10.1016/j.intermet.2024.108273.

[5] J. Lu, L. Li, Y. Chen, X. Liu, X. Zhao, F. Guo, P. Xiao, Y-Hf co-doped AlCoCrFeNi high-entropy alloy coating with superior oxidation and spallation resistance at 1100 °C, Corrosion Sci. 182 (2021) 109267, https://doi.org/10.1016/j.corsci.2021.109267.

[6] J. Lu, H. Zhang, L. Li, Y. Chen, X. Liu, X. Zhao, F. Guo, Y-Hf co-doped AlCoCrFeNi2.1 eutectic high-entropy alloy with excellent oxidation and spallation resistance under thermal cycling conditions at 1100 °C and 1200 °C, Corrosion Sci. 187 (2021) 109515, https://doi.org/10.1016/j.corsci.2021.109515.

[7] J. Lu, Y. Chen, H. Zhang, N. Ni, L. Li, L. He, R. Mu, X. Zhao, F. Guo, Y/Hf-doped AlCoCrFeNi high-entropy alloy with ultra oxidation and spallation resistance, Corrosion Sci. 166 (2020), https://doi.org/10.1016/j.corsci.2019.108426.

[8] J. Lu, Y. Chen, H. Zhang, L. Li, L. Fu, X. Zhao, F. Guo, P. Xiao, Effect of Al content on the oxidation behavior of Y/Hf-doped AlCoCrFeNi high-entropy alloy, Corrosion Sci. 170 (2020) 108691, https://doi.org/10.1016/j.corsci.2020.108691.

[9] T.M. Butler, M.L. Weaver, Oxidation behavior of arc melted AlCoCrFeNi multi-component high-entropy alloys, J. Alloys Compd. 674 (2016) 229–244, https://doi.org/10.1016/j.jallcom.2016.02.257.

[10] M. Jawańska, J. Dąbrowa, M. Bik, G. Cieślak, P. Jeleń, K. Mroczka, J. Wyrwa, Rogal, A. Gil, M. Galetz, J. Jedliński, Role of the rare-earth elements effect in transforming the oxidation behavior of AlxCoCrFeNi high entropy alloys, Corrosion Sci. 222 (2023), https://doi.org/10.1016/j.corsci.2023.111412.

[11] M. Jawańska, J. Dąbrowa, M. Bik, L. Rogal, G. Cieślak, A. Gil, M. Galetz, J. Jedliński, Effect of Hf on high-temperature oxidation behavior of chromia-forming AlxCoCrFeNi alloys, Corrosion Sci. 240 (2024), https://doi.org/10.1016/j.corsci.2024.112455.

[12] K. Ma, F. Tang, J.M. Schoenung, Investigation into the effects of Fe additions on the equilibrium phase compositions, phase fractions and phase stabilities in the Ni-Cr-Al system, Acta Mater. 58 (2010) 1518–1529, https://doi.org/10.1016/j.actamat.2009.10.059.

[13] C.S. Giggins, F.S. Pettit, Oxidation of Ni-Cr-Al alloys between 1000° and 1200°C, J. Electrochem. Soc. 118 (1971) 1782, https://doi.org/10.1149/1.2407837.

[14] Y. Hong, M. Beyramali Kivy, M. Asle Zaeem, Competition between formation of Al_2O_3 and Cr_2O_3 in oxidation of Al0.3CoCrCuFeNi high entropy alloy: a first-principles study, Scripta Mater. 168 (2019) 139–143, https://doi.org/10.1016/j.scriptamat.2019.04.041.

[15] L. Yang, Z. Zhou, R. Yang, J. Wang, M. Chen, Y. Qiao, S. Zhu, F. Wang, Effect of Al and Cr on the oxidation behavior of nanocrystalline coatings at 1050 °C, Corrosion Sci. 200 (2022) 3–10, https://doi.org/10.1016/j.corsci.2022.110191.

[16] R. Prescott, M.J. Graham, The Formation of aluminum oxide scales on high-temperature alloys, Oxid. Metals 38 (1992) 233–254.

[17] N. Birks, G.H. Meier, F.S. Pettit, Introduction to the High Temperature Oxidation of Metals, Cambridge university Press, Cambridge, 2006, https://doi.org/10.2277/0521480426.

[18] M.P. Brady, I.G. Wright, B. Gleeson, Alloy design strategies for promoting protective oxide-scale formation, Jom 52 (2000) 16–21, https://doi.org/10.1007/s11837-000-0109-x.

[19] T.J. Nijdam, L.P.H. Jeurgens, W.G. Sloof, Modelling the thermal oxidation of ternary alloys - compositional changes in the alloy and the development of oxide phases, Acta Mater. 51 (2003) 5295–5307, https://doi.org/10.1016/S1359-6454(03)00381-1.

[20] T.J. Nijdam, W.G. Sloof, Modelling of composition and phase changes in multiphase alloys due to growth of an oxide layer, Acta Mater. 56 (2008) 4972–4983, https://doi.org/10.1016/j.actamat.2008.06.010.

[21] R.C. Reed, The Superalloys Fundamentals and Applications, Cambridge University Press, Cambridge, 2006, https://doi.org/10.1017/CBO9780511541285.

[22] X. Sun, L. Zhang, Y. Pan, X. Wang, Z. Huang, L. Jiang, Microstructural evolution during cyclic oxidation of a Ni-based singe crystal superalloy at 1100 °C, Corrosion Sci. 162 (2019) 108216, https://doi.org/10.1016/j.corsci.2019.108216.

[23] X. Sun, P. Zhang, J. Moverare, X. Li, L. Cui, R. Lin, Materials & Design Impeding the γ' depletion during the interdiffusion between bond coatings and superalloys via introduction of tantalum in bond coatings, Mater. Des. 227 (2023) 111792, https://doi.org/10.1016/j.matdes.2023.111792.

[24] A.A. Luo, Material design and development: from classical thermodynamics to CALPHAD and ICME approaches, Calphad Comput. Coupling Phase Diagrams Thermochem. 50 (2015) 6–22, https://doi.org/10.1016/j.calphad.2015.04.002.

[25] F. Gesmundo, F. Viani, Application of Wagner's theory to the parabolic growth of oxides containing different kinds of defects: II . Doped oxides, J. Electrochem. Soc. 128 (1981) 470–479, https://doi.org/10.1149/1.2127440.

[26] X. Sun, L. Zhang, Y. Pan, Z. Huang, L. Jiang, Investigation of breakaway oxidation kinetics of nickel-base single crystal superalloys: modeling and experiments, Mater. Today Commun. 32 (2022) 103893, https://doi.org/10.1016/j.mtcomm.2022.103893.

[27] J. Peng, X. Fang, V. Marx, U. Jasnau, M. Palm, Isothermal oxidation behavior of Tribaloy TM T400 and T800, npj Material Degradation 38 (2018) 1–7, https://doi.org/10.1038/s41529-018-0060-3.

[28] D. Monceau, B. Pieraggi, Determination of parabolic rate constants from a local analysis of mass-gain curves, Oxid. Metals 50 (1998) 447–493.

[29] D.J. Young, High Temperature Oxidation and Corrosion of Metals, second ed., Elsevier Inc., 2016 https://doi.org/10.1016/C2014-0-00259-6.

[30] T. Nakagawa, I. Sakaguchi, N. Shibata, K. Matsunaga, T. Mizoguchi, T. Yamamoto, H. Haneda, Y. Ikuhara, Yttrium doping effect on oxygen grain boundary diffusion in α-Al2O3, Acta Mater. 55 (2007) 6627–6633, https://doi.org/10.1016/j.actamat.2007.08.016.

[31] B.A. Pint, Experimental Observations in Support of the Dynamic-Segregation Theory to Explain the Reactive-Element Effect, vol. 45, 1996, pp. 1–37.

[32] D. Naumenko, B.A. Pint, W.J. Quadakkers, Current thoughts on reactive element effects in alumina-forming systems: in memory of john stringer, Oxid. Metals 86 (2016) 1–43, https://doi.org/10.1007/s11085-016-9625-0.

[33] J.L. Smialek, Invited Review Paper in Commemoration of over 50 Years of Oxidation of Metals : Alumina Scale Adhesion Mechanisms : A Retrospective Assessment, Springer US, 2022, https://doi.org/10.1007/s11085-021-10091-2.

[34] A. Sato, Y.L. Chiu, R.C. Reed, Oxidation of nickel-based single-crystal superalloys for industrial gas turbine applications, Acta Mater. 59 (2011) 225–240, https://doi.org/10.1016/j.actamat.2010.09.027.

[35] I. Barin, O. Knacke, O. Kubaschewski, Thermochemical Properties of Inorganic Substances, 1977, p. 1977 (Supplement). By, i.

[36] Z. Zhao, J. Wang, M. Chen, J. Zhang, F. Wang, D.J. Young, Comparative study on the initial oxidation behavior of conventional and nanocrystalline MCrAlY coatings - effect of microstructure evolution and dynamic mechanisms, Acta Mater. 239 (2022) 118264, https://doi.org/10.1016/j.actamat.2022.118264.

[37] Y. Chen, X. Zhao, P. Xiao, Effect of microstructure on early oxidation of MCrAlY coatings, Acta Mater. 159 (2018) 150–162, https://doi.org/10.1016/j.actamat.2018.08.018.

[38] N. Ta, L. Zhang, Q. Li, Z. Lu, Y. Lin, High-temperature oxidation of pure Al: kinetic modeling supported by experimental characterization, Corrosion Sci. 139 (2018) 355–369, https://doi.org/10.1016/j.corsci.2018.05.013.